Spring 2016

Active 2D Microrheological Studies in Freely-Suspended Smectic Liquid Crystal Films

Kyle R. Ferguson
University of Colorado Boulder, kyle.ferguson@colorado.edu

Active 2D Microrheological Studies in Freely-Suspended Smectic Liquid Crystal Films

by

Kyle Ferguson

A thesis submitted to the faculty of the
University of Colorado in partial fulfillment
of the requirements for the award of
departmental honors in the
Department of Physics
2016

This thesis entitled:
Active 2D Microrheological Studies in Freely-Suspended Smectic Liquid Crystal Films
written by Kyle Ferguson
has been approved for the Department of Physics

_____

Joseph Maclennan

_____

John Cumalat

_____

Mark Hoefer

Date _____

The final copy of this thesis has been examined by the signatories, and we find that both the content and the form meet acceptable presentation standards of scholarly work in the above mentioned discipline.

Ferguson, Kyle (B.S., Engineering Physics)

Active 2D Microrheological Studies in Freely-Suspended Smectic Liquid Crystal Films

Thesis directed by Prof. Joseph Maclennan

Thin, freely-suspended smectic liquid crystal films, due to their layered structure, provide an ideal system with which to study two dimensional (2D) hydrodynamics. We have performed some of the first experimental visualizations of actively-driven 2D flow fields, and compared these flow fields to predictions made by theoretical models. First, an experiment testing the flow field generated by a disk-shaped inclusion moving laterally in a film is described. Then an experiment testing the flow field generated by a thin nozzle injecting fluid at a quick rate into a large reservoir is detailed. Results are consistent with the idea that 2D fluids exhibit strong coupling with surrounding bulk fluid.

Acknowledgements

Besides myself, the completion of this work is due to many others, who have generously provided me with aid, motivation, and sanity checks along the way. Much thanks to Cheol Park, who was always available with a suggestion for what to do when I hit a roadblock, and whose levity and sense of humor made such roadblocks seem more surmountable. Thanks to my advisor Joe Maclennan, whose IDL programming abilities saved me weeks' worth of work and whose seemingly infinite patience with me should probably qualify him for a sainthood. I would be remiss to not thank the graduate students I've worked with: Zhiyuan Qi, whose love for learning birthed the main concepts for both of my experiments, and Adam Green, who was always so graciously willing to offer assistance. Thanks to the other undergrads, Kate Wachs, Kyle Meienberg, and Kaitlyn Parsons, for always providing company and camaraderie when I grew frustrated with what I was working on. Lastly, thank you to the Soft Materials Research Center and the Undergraduate Research Opportunities Program for funding this work.

Go Buffs!

Contents

Figures

Figure

Chapter 1

An Introduction to Liquid Crystals and 2D Hydrodynamics

Liquid crystals (LCs) are materials which exhibit properties of both the liquid and the solid phases. Because of this, they behave in unique ways that allow the study of many physical properties difficult to come by in other systems. Specifically, LCs can form thin, freely-suspended films (somewhat similar to the soap films one might create to blow bubbles). Because the surface areas of these films are many orders of magnitude larger than their thicknesses, the films are ideal systems for the study of two-dimensional (2D) hydrodynamics. Results from these studies can be applied to more complex systems, such as those of a protein moving through a biological membrane.

This thesis is organized in the following way. Chapter 1 discusses all relevant background on LCs and 2D hydrodynamics necessary to understand the work that I have performed. Chapters 2 and 3 each discuss a separate experiment I have performed to determine how 2D fluids respond to actively-driven flow.

1.1 Smectics and Their Uses

The study of LCs dates back to 1888, when chemist Friedrich Reinitzer discovered that a cholesterol-based material he was studying had two separate melting points: the first from solid to LC, and the second from LC to true liquid [29]. For the first time, a phase beyond the three traditional phases (solid/liquid/gas) had been observed. As LC research continued, it was determined that there exist various sub-phases within the liquid crystal umbrella. Generally, LCs are divided into two groups: thermotropic (those whose phase depends on temperature) and lyotropic

(those whose phase depends on relative concentration of two or more materials). My research has not focused on any lyotropic LCs, and thus they will not be discussed in any more depth.

Thermotropic LCs generally comprise rod-shaped molecules, and they fall into one of three main groups: nematic, chiral, or smectic [4, 20, 21]. Nematic LCs exhibit a bulk uniform orientational order, but no positional order. Chiral LCs are much the same (and in fact are often called chiral nematic), except the orientation rotates with distance, leading to the chiral handedness. Smectic LCs, on the other hand, exhibit both orientational and positional order. Smectics form discrete layers, within which individual molecules are for the most part confined; however, molecules are free to flow like a liquid within each layer.

Even within the sub-group of smectics, it is possible to divide further. In this thesis, I describe work performed with both Smectic A (SmA) and Smectic C (SmC) LCs. For materials in the SmA phase, the average orientation of the rod-shaped molecules is directly normal to the individual layers. In the SmC phase, the molecules are on average oriented at some angle relative to this normal. Molecular representations of these three main thermotropic phases are shown in Fig. 1.1.

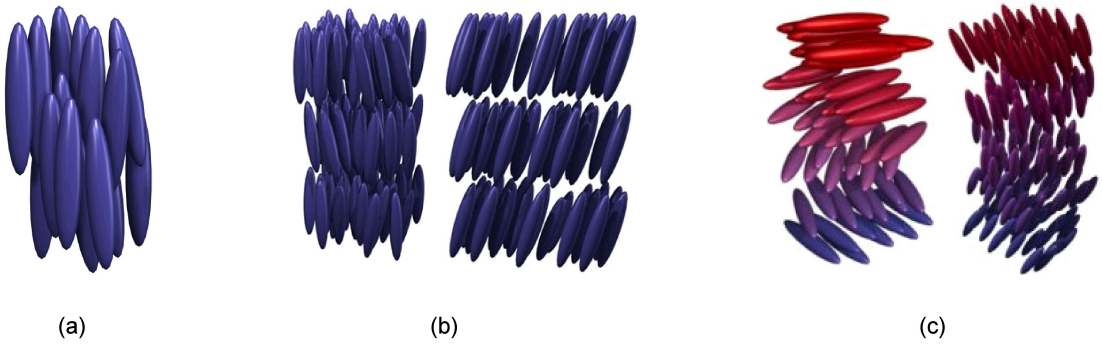

Figure 1.1: Molecular representations of the three main thermotropic LC phases: nematic (a), smectic (b), and chiral (c). In (b), the smectic A phase is shown on the left and smectic C on the right. In (c), we see that chiral phases can exhibit two different kinds of chirality. Figure from [1].

Smectics as a whole, due to their layered structure, lend themselves well to forming thin, freely-suspended films. These films are generally on the nanometer-to-micron-scale in thickness, and are stable over long time scales due to the surface tension that holds them up. They can

be created on film holders of various sizes and shapes, depending on what is necessary for the experiment. For instance, one film holder may be a glass cover slip with a 3 mm diameter hole drilled in it; another may be a piece of acrylic with a 1 cm $\times$ 1 cm square aperture laser-etched into it. As we shall see in chapter 3, even more complex shapes can be created. Generally, any solid material will work for the film holder as long as it contains smooth edges along the film boundary. The films are drawn by coating the edge of a glass cover slip with the smectic material, then drawing the cover slip over the film holder at a slow, steady rate. This is demonstrated visually in Fig. 1.2.

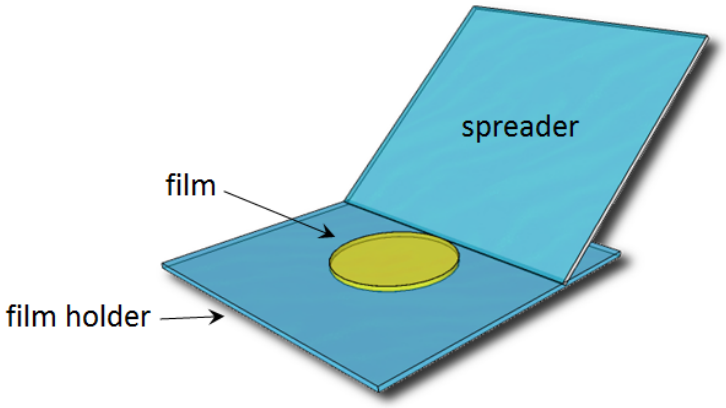

Figure 1.2: Schematic showing how smectic films are created. The edge of a spreader is coated in the smectic LC, then drawn across a hole in the film holder. Though films are often circular, any geometry is technically possible to create.

Often, we study inclusions in smectic films rather than the films themselves; this is necessary, as the inclusions act as visualizers for long-range flow. Generally, for these inclusions we use smectic islands - thicker, pancake-like regions of the film, like those shown in Fig. 1.3. While islands can be generated spontaneously, this is more common to SmC materials; in SmA materials, we must actively create them. There are two methods of doing this. In the first, we blow air on the meniscus of the film, pushing excess smectic material into the center. In the second, we place the film in a chamber with smoke and wait for ash particles to become embedded in the film. Small islands tend to nucleate around these particles, making this method especially useful for long-range flow field visualization.

Studies of these films have two main applications. First, smectic LCs are useful in the study

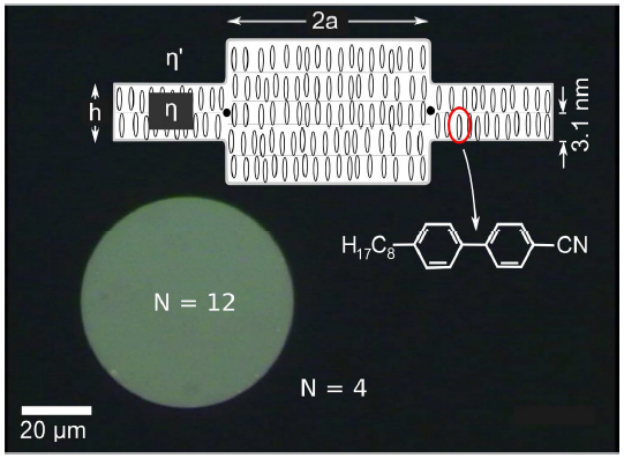

Figure 1.3: Schematic showing the molecular structure of smectic islands (specifically for the SmA material 8CB) overlaid upon a reflective microscopic image of an $N = 12$-layer island in an $N = 4$-layer film.

of 2D hydrodynamics. By the very nature of the films, the individual molecules are confined to a single layer, and thus have only two degrees of freedom in movement. Additionally, the large surface-area-to-thickness ratio means that any flow between layers is still negligible compared to the lateral flow. Second, smectic LCs act as ideal approximations to biological membranes. Both are extremely thin fluids well in the 2D hydrodynamic regime; but while biological membranes are complex, with many competing processes, smectic films have the benefit of constant viscosity and uniform thickness. On top of that, we can experimentally control the types of inclusions in the films.

1.2 2D Hydrodynamics Background

The fundamental building blocks of all fluid dynamics are the Navier-Stokes Equations; generalizations of Newton's Second Law applied to fluids. However, when applying the linearized Navier-Stokes Equations (often just called the Stokes Equations) to 2D fluids, one runs into what is known as the Stokes Paradox. This is a mathematical concept with many different experimental interpretations; the most useful for our purposes is the following: according to the Stokes Equations, the mobility μ ($\propto \frac{D}{\eta}$, where D is the diffusion coefficient and η is the dynamic viscosity) of

an inclusion embedded in a 2D fluid diverges as the size of the fluid increases. This is, of course, absurd; there must be a physical constraint to impose on the system and limit the mobility to a finite value.

Saffman and Delbrück (SD) [30] were the first to resolve the paradox as it related to the dynamics of inclusions. They determined that one can limit the inclusion's mobility to a finite value if the effect of the bulk fluid above and below the 2D membrane (usually air) is taken into account. The inclusion exchanges momentum with this bulk fluid, decreasing its mobility from that in the true 2D case. Note that SD specifically focused on the hydrodynamics of biological membranes; experimental confirmation that their results are applicable to all 2D fluids did not come until later (as we shall see below). The SD expression for mobility μ is

$$\mu = \frac{1}{4\pi\eta_m}\left[\log\left(\frac{2l_S}{a}\right) - \gamma_E\right], \tag{1.1}$$

where η_m is the dynamic viscosity of the membrane, a is the radius of the inclusion, γ_E is the Euler constant, and l_S is the Saffman length,

$$l_S = \frac{h\eta_m}{2\eta_f}, \tag{1.2}$$

where h is the thickness of the membrane and η_f is the dynamic viscosity of the surrounding bulk fluid. One limitation of SD's result is that it is only valid for inclusions of size $a \ll l_S$.

Hughes, Pailthorpe, and White (HPW) [13] later expanded the SD result to determine analytically the mobility of an inclusion of any size embedded in a 2D membrane. They used the linearized Navier-Stokes equations to calculate the drag on a cylindrical inclusion moving in a membrane; from this drag, they were then able to calculate the diffusion coefficient and thus, the mobility. However, the HPW corrections to the original model are cumbersome; Petrov and Schwille [25] developed an accurate approximation that is much simpler computationally. Later, Petrov et al. [24] experimentally confirmed SD-HPW theory in an experiment measuring the translational and rotational diffusion of inclusions in a lipid membrane.

Other refinements have been developed for SD-HPW theory to remove some of the assumptions made in the model. For example, in the SD-HPW model, it is assumed that the membrane extends infinitely in all planar directions. Carbajal-Tinoco et al. [3] tested an extended model for the diffusion of inclusions near a boundary. They found that an inclusion's diffusion coefficient decreases the closer the inclusion gets to a boundary. Additionally, they found that separate diffusion coefficients exist for diffusion parallel to and perpendicular to the boundary, confirming a large background of theoretical work [10, 2, 23, 5].

In another refinement, Oppenheimer and Diamant [18] extended the theory to account for inclusions far from a wall, but still in a bounded membrane. They found refined diffusion coefficients that shrank faster than similarly-sized inclusions in infinite membranes. They also found that the transverse diffusion has a dependence on the overall concentration of inclusions, although the longitudinal diffusion does not. Later [19], the two developed a theory allowing for immobile inclusions in the membrane, finding that the interaction between a mobile and an immobile inclusion falls off much quicker with distance than the interaction between two mobile inclusions.

Experiments have verified that the SD-HPW framework is applicable to many 2D fluids (and not just lipid membranes, as originally discussed by SD). Prasad and Weeks [27] worked specifically with soap films, devising an experiment to determine whether they acted more as 2D fluids or 3D fluids. They found a 2D-to-3D transition for $h/d > 7 \pm 3$ (where h is film thickness and d is the diameter of the inclusions), beyond which single particles diffused faster than 2D hydrodynamics theory predicted. However, they found that the total flow field of the film was as predicted by theory for all values of h/d.

Nguyen et al. [17] examined the mobility of isolated inclusions roughly the size of the Saffman length embedded in SmA films. In this quasi-2D regime between full 2D behavior and 3D behavior, it is the HPW corrections that dominate the theoretical predictions for behavior. The group confirmed that SD-HPW theory accurately describes the diffusion of inclusions in this regime for smectic films; their results are shown in Fig. 1.4.

Eremin et al. [9] performed an experiment using smectic films, determining the regime for

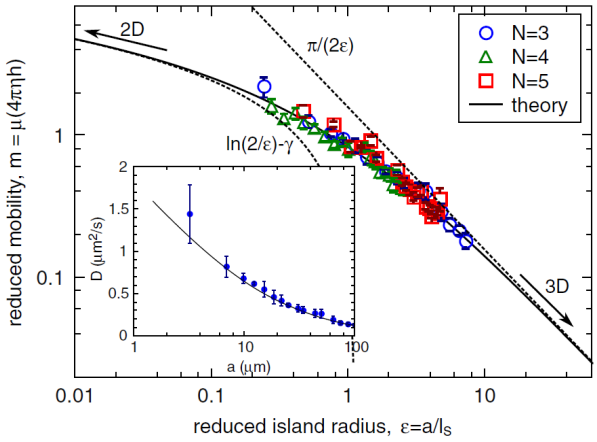

Figure 1.4: Reduced mobility as a function of inclusion size. The solid curve represents the SD-HPW predictions, while the dotted curve on the left represents SD predictions without the HPW corrections. The dotted curve on the right represents the pre-SD theory, in which the mobility increases without bound (the Stokes Paradox). It is apparent that SD-HPW theory is accurate for describing the mobility of single inclusions embedded in smectic films. From Nguyen et al. [17].

which SD-HPW theory dominates and the regime for which confinement effects dominate. The scientists tilted their films at an angle such that the inclusions would flow downwards under gravity's influence. By measuring their motion, they found that as the film width decreases to smaller than the Saffman length, hydrodynamic interactions stop being dominated by air coupling and instead become dominated by confinement effects. They also found that flow fields fell off significantly slower than 3D theory predicted. These experiments demonstrate that SD-HPW theory extends beyond biological membranes to general 2D fluids.

Though experiments and work on the diffusion of inclusions in smectic films are not directly related to the flow-based studies I have performed, it is imperative to discuss this 2D hydrodynamics background since the theories I work with to predict flow in my films build upon the SD-HPW framework. These are discussed in greater depth in their respective chapters.

Chapter 2

Mapping the Flow Field Generated by an Inclusion Moving Laterally in a Film

Note: Much of this chapter is adapted from "Active Microrheology of Smectic Membranes," on which I am a co-author. The paper is currently under review at Physical Review E.

While many studies of the motion of individual inclusions in 2D membranes have been carried out, the literature is surprisingly lacking in experimental mapping of the flow fields generated by the motion of these inclusions. The following chapter details an experiment in which we map the flow field generated by an actively-driven inclusion moving in a smectic film and compare the observed results to a theoretical model. A circular post is oscillated laterally in the film, and the responsive motion of tracer particles around the post is analyzed to determine the flow field.

2.1 Theoretical Model

The theoretical model used is a generalization of a theory developed by Levine and MacKintosh (LM) [15]. The two built upon the SD-HPW framework to determine the response of the film itself to the motion of an inclusion within the film. More specifically, LM derived the parallel and perpendicular response functions ($\alpha_{\parallel}$ and $\alpha_{\perp}$, respectively) of the film due to a point force acting in the film. Mathematically, these are Green's functions that solve the Stokes Equations. The response functions are given by

$$\alpha_{\parallel}(\chi) = \frac{1}{4\pi\eta h}\left[\frac{\pi}{\beta}H_1(\beta) - \frac{2}{\beta^2} - \frac{\pi}{2}[Y_0(\beta) - Y_2(\beta)]\right] \tag{2.1}$$

and

$$\alpha_{\perp}(\chi) = \frac{1}{4\pi\eta h}\left[\pi H_0(\beta) - \frac{\pi}{\beta}H_1(\beta) + \frac{2}{\beta^2} - \frac{\pi}{2}[Y_0(\beta) - Y_2(\beta)]\right], \tag{2.2}$$

where χ is the separation between the point of interest and the point at which the force is applied, η is the viscosity of the material, h is the thickness of the membrane, and $\beta = \chi/l_S$. Note that H_i are Struve functions and Y_i are Bessel functions of the second kind. Experimental testing of LM theory has been limited; Qi et al. [28] indirectly tested LM theory in one direction in an experiment determining the mutual mobilities of islands in smectic liquid crystal films, but a full mapping of the flow fields generated by actively-driven inclusions in smectic films has not yet been performed.

In reality, we of course have objects of finite size rather than point forces. We can generalize the LM response functions to this situation by employing a technique developed by Tatiana Kuriabova (paper not yet published). For the case of a circular inclusion moving in close proximity to a straight boundary (chosen for the sake of this description to run along the y-direction), the velocity response of the film is given by

$$v^{\mu}(\mathbf{x}) = \int_0^{2\pi} f^{\nu}(\phi)\alpha_{\mu\nu}\Big(\mathbf{x} - \mathbf{x}'(\phi)\Big)\, d\phi + \int_{-\infty}^{+\infty} g^{\nu}(y)\alpha_{\mu\nu}\Big(\mathbf{x} - \mathbf{x}'(y)\Big)\, dy. \tag{2.3}$$

In this equation, $\mu, \nu = x, y$. The vectors $\mathbf{x}'(\phi) = a\cos\phi\hat{x} + a\sin\phi\hat{y}$ and $\mathbf{x}'(y) = \Delta\hat{x} + y\hat{y}$ (where a is the radius of the inclusion and Δ is the distance between the boundary and the center of the inclusion) describe the edge of the inclusion and the straight boundary, respectively. The strengths of the point forces along the edges, $f^{\nu}(\phi)$ and $g^{\nu}(y)$, are initially unknown and must be solved for. $\alpha_{\mu\nu}$ is the LM response tensor, given by

$$\alpha_{\mu\nu}(\mathbf{x}) = \alpha_{\parallel}(|\mathbf{x}|)\hat{x_{\mu}}\hat{x_{\nu}} + \alpha_{\perp}(|\mathbf{x}|)[\delta_{\mu\nu} - \hat{x_{\mu}}\hat{x_{\nu}}]. \tag{2.4}$$

By implementing no-slip boundary conditions along both edges, we can determine $f^{\nu}(\phi)$ and $g^{\nu}(y)$. The equation must be solved numerically; thus, the integrals are discretized, with the edges

broken up into a multitude of so-called Levineslets, portions of extremely small size that can be approximated as points. Additionally, the infinite bounds in the second integral are set to $\pm 10\Delta$ since points beyond this have negligible effect. Because the Stokes Equations are linear, we can superpose the response due to each of these Levineslets and solve for the total flow field. This is known as the boundary element method.

2.2 Experiment

I now describe the experimental setup we used to test the generalized LM model. We used two different film holders: the first a circular film holder 1 cm in diameter (to test flow far from any boundaries), and the second a 10 mm $\times$ 4 mm rectangular film holder (to test flow for an inclusion moving in close proximity to a straight, fixed boundary). The smectic material we used is 8CB (4′-n-octyl-4′-cyanobiphenyl, Sigma-Aldrich), which has the following phase diagram: Crystal $\rightarrow$ (21.5 °C) $\rightarrow$ Smectic A $\rightarrow$ (33.5 °C) $\rightarrow$ Nematic $\rightarrow$ (40.5 °C) $\rightarrow$ Isotropic. We see that 8CB is in the smectic A phase at room temperature. The material's molecular structure is shown in Fig. 2.1. 8CB has a viscosity of $\eta = 0.052$ Pa $\cdot$ s [32] and a density of $\rho \approx 0.96$ g/cm^3 [14], while each layer is 3.17 nm thick [6]. Given that the viscosity of the surrounding air is $\eta' = 1.827 \times 10^{-5}$ Pa $\cdot$ s [8], and that standard films are between two and six layers thick, we generally have Saffman lengths between 9 and 27 μm.

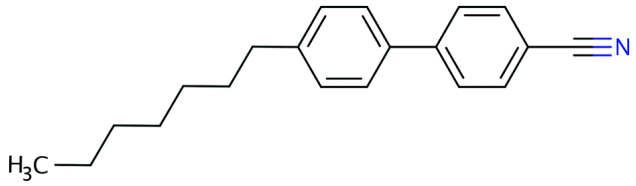

Figure 2.1: Molecular structure of 8CB. From [22].

Once a film has been drawn, ash particles are deposited on it to act as flow visualizers, as described in chapter 1. The film is placed beneath a microscope and the post is raised so that the tip just pierces the film (note that the post is coated in a small amount of 8CB in order to do this without popping the film). The post is attached to a magnet atop a leaf spring; an oscillatory

current signal is sent through a solenoid to drive the post back and forth. We drive the post with a 2 Hz triangle wave, with a peak-to-peak amplitude of approximately 50 μm. The film is observed using reflective light microscopy, and video is captured at 60 frames per second on a Phantom v12.1 video camera with 1280×800 resolution. The videos are decomposed into image stacks, which are run through a particle-imaging velocimetry program in order to determine the instantaneous flow field. The entire setup is depicted visually in Fig. 2.2. Note that initially, we used a slightly different setup in which the post was attached to a piezoelectric plate. This would occasionally cause electrostatic repulsion of the tracer particles from the post, so we changed to the setup shown.

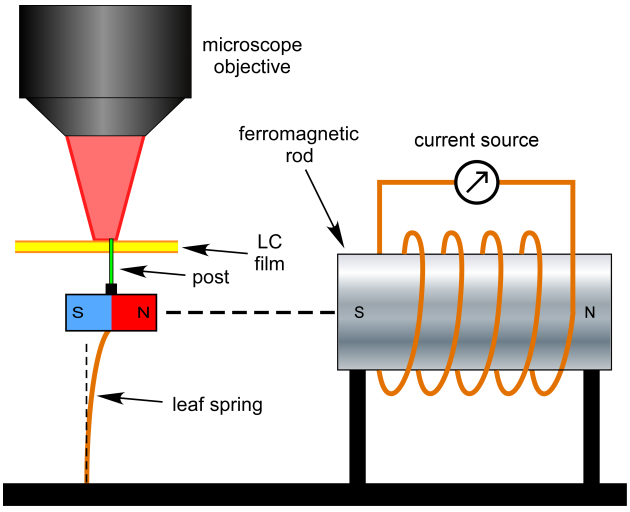

Figure 2.2: Experimental setup to test the generalized LM model. A thin, metal post is mounted on a leaf spring and raised such that it just pierces the film. The post is driven back and forth by a solenoid, and the film is observed via reflective light microscopy.

2.3 Results

We mapped the flow field in four separate cases: two in the center of the circular film (with different post sizes) and two near a straight film boundary (for motion parallel and perpendicular to the boundary).

2.3.1 Center of the Film

We first examined the case of a post of radius $a = 8.1$ Saffman lengths moving laterally in an $N = 3$-layer film. A reflective microscopic image of this situation is shown in Fig. 2.3 (a). Note that the small white dots are the ash particles embedded in the film, each with a small smectic meniscus surrounding it. There is an excess of 8CB around the edge of the post; however, the movement of the post is slow (Re $\approx 10^{-5}$), so this excess material moves with the post without becoming deformed, essentially acting to extend the radius. The post itself is of variable brightness because its uneven top reflects light in different directions, but since this part of the post is not in direct contact with the film, the effect on the flow is negligible. The instantaneous velocity of the post is in the positive y-direction, as can be seen by the experimentally observed flow field plotted in Fig. 2.3 (b). Fig. 2.3 (c) shows the LM-predicted flow field. Qualitatively, it appears that theory and experiment are in agreement.

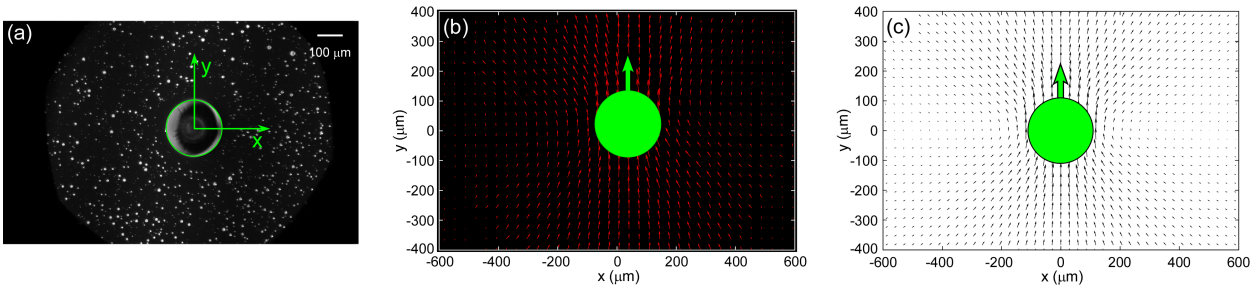

Figure 2.3: (a) Reflective microscopic image of a post of radius $a = 8.1$ Saffman lengths moving in an $N = 3$-layer film. The y-axis represents the direction of instantaneous velocity, which has the value $v_0 = 143$ μm/sec. The small white dots are ash particles surrounded by a small smectic meniscus, used to visualize the flow. (b) Experimentally-observed flow field for the same situation. The flow field is determined using a particle-imaging velocimetry program developed by a graduate student at CU. The green arrow represents the direction of post movement. (c) LM-predicted flow field for a disk-shaped inclusion the same thickness as the film 8.1 Saffman lengths in radius. Qualitatively, we see that theory and experiment agree.

It is difficult to compare the entire observed flow field to that predicted by our generalized LM model. Rather, we examine flow along the y-axis (along the direction of post motion) and x-axis (perpendicular to the direction of post motion). Velocity vs. distance from the center of the post along these two lines are plotted in Fig. 2.4 (a) and (b), respectively. It is evident that the flow

is anisotropic; flow falls off much quicker with distance in the x-direction than in the y-direction. In these plots, the green bar represents the physical size of the post; scales are normalized such that the radius and velocity of the post are both equal to 1. The red circles represent experimental data, with the error bars determined by statistical averaging over 10 cycles of the post in the same point of its oscillation. The solid black line represents the theoretical LM predictions for flow generated by a disk-shaped inclusion the same thickness as the membrane moving within it. The blue line represents the velocity of the air moving a distance below the film, as generated by the post extending below the film. The dashed black line represents a best fit of the data using a model that is a linear combination of both the LM flow in the film and the flow in the air, normalized such that the velocity is equal to 1 at the post edge.

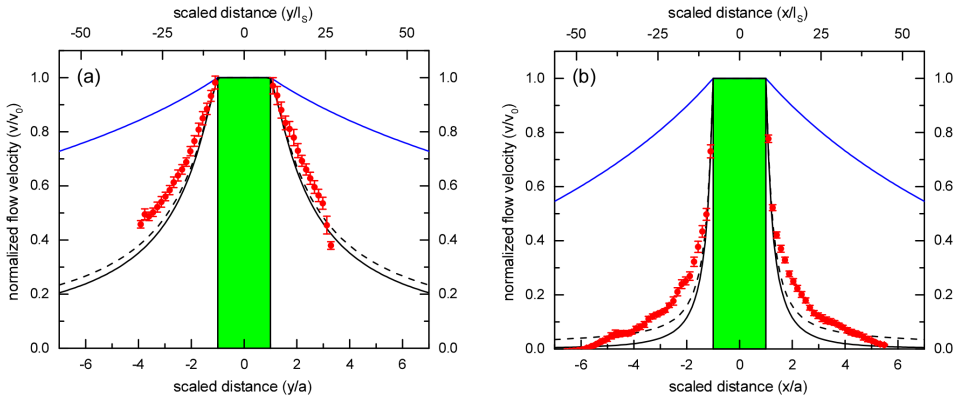

Figure 2.4: Magnitude of velocity vs. distance from the center of the post is plotted along the y-axis (a) and x-axis (b). The red points are experimental data, with error bars determined by taking the standard deviation of the mean of each point after averaging over 10 oscillation cycles. The green rectangle represents the physical size of the post. The solid black line represents the generalized LM-model predictions; note that it under-predicts the observed velocities. The solid blue curve represents the velocity profile of the air a distance beneath the film. The dashed black curve represents a best fit to the data that linearly combines the LM and air curves. In this case, the best fit is 94.5 % LM flow and 5.5% air flow.

We see that the theoretical LM predictions for velocity fall off faster with distance than the observed velocities. This is due to additional flow in the air beneath the film generated by the extension of the post. While the LM model accounts for coupling between the air and film, it assumes that the object moving in the membrane exerts a force only in said membrane. The motion

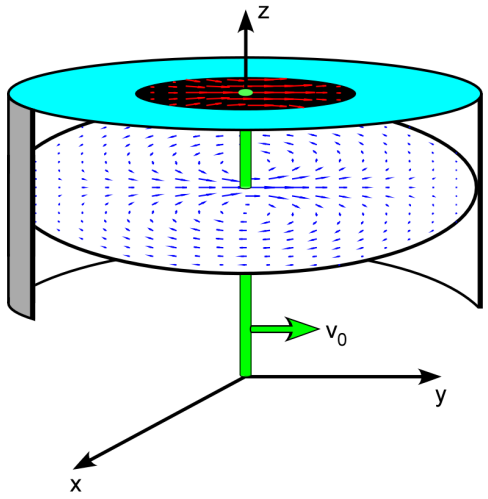

Figure 2.5: Representation of air flow boosting flow in film. The flow field in the air is calculated by treating the post as an infinite cylinder. Because the air beneath the film moves in the same direction as the film, there is additional momentum-exchange unaccounted for in our generalized LM model, leading to faster-than-predicted observed velocities.

of the air below the film in our experiment introduces an extra source of momentum-exchange to the film/air system, boosting the flow in the film. To determine the flow field in the air, we treat the post as an infinite cylinder and follow the derivation in Happel and Brenner [12] (not reproduced here). A schematic of this is shown in Fig. 2.5. Unfortunately, the complete flow field in the film can not be solved for, since the air flow is only excited below the film and not above. This is why we have introduced the fit (the dashed black curve). While we do not expect a simple linear combination of the two contributions to fully describe the behavior we observe, this gives us a good idea of just how much the air contributions are a factor. For the case of a post 8.1 Saffman lengths in radius, we find that the best fit comprises 94.5 % LM flow and 5.5% air flow. It is important to note that the velocity is always positive; that is, always in the same direction as the movement of the post. As expected, we do not observe any recirculation.

We also observed the case of a post 2.58 Saffman lengths in radius moving in an $N = 3$-layer film. We can see from the plots in Fig. 2.6 that the discrepancy between theory and experiment is much more pronounced for this smaller post the best fit line comprises 66% LM flow and 34% air flow. This is to be expected; the theoretical predictions for the air flow fall off much slower than

those for film flow when the post is smaller (normalized to the length scale of post radius), and thus the relative boost to LM flow is larger.

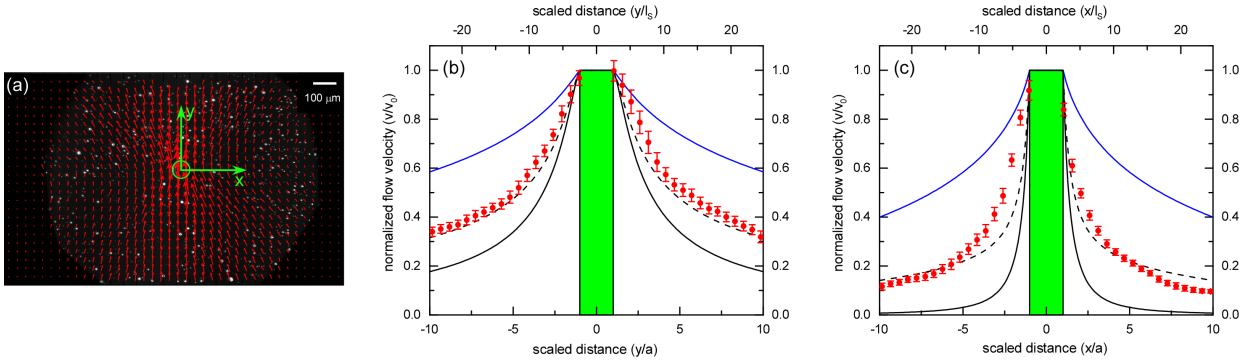

Figure 2.6: (a) Experimentally observed flow field overlaid upon a reflective microscopic image of the post in the film. (b,c) Magnitude of velocity vs. distance from the center of the post is plotted along the y-axis (b) and x-axis (c). All visual conventions are the same as in Fig. 2.4. The discrepancy between theory and experiment is larger for the smaller post size, with the best fit given by 66% LM flow and 34% air flow.

2.3.2 Near a Straight Boundary

In addition, separate flow fields were mapped for a post moving parallel to and perpendicular to a straight film boundary. In this case, both the post edge and the boundary are broken up into Levineslets, and no-slip boundary conditions are imposed on both.

The experimentally-observed flow field for a 3.58 Saffman length radius post moving parallel to the boundary of an $N = 5$-layer film is overlaid upon a reflective microscopic image in Fig. 2.7 (a). The center of the post is 232 μm (10.32 l_S) from the edge of the meniscus. Fig. 2.7 (b) shows the LM-predicted flow field for a disk-shaped inclusion of the same size moving parallel to a straight boundary at the same distance. The gray area represents the film meniscus, while the cyan area represents the actual glass boundary of the film holder. Fig. 2.8 shows velocity scans along the y-axis (a) and x-axis (b) for this case.

Figs. 2.9 and 2.10 show the same for an inclusion moving perpendicular to the boundary; here, the post is 5.59 Saffman lengths in radius, the film is 3 layers thick, and the center of the post is 258 μm (19.10 l_S) from the edge of the meniscus.

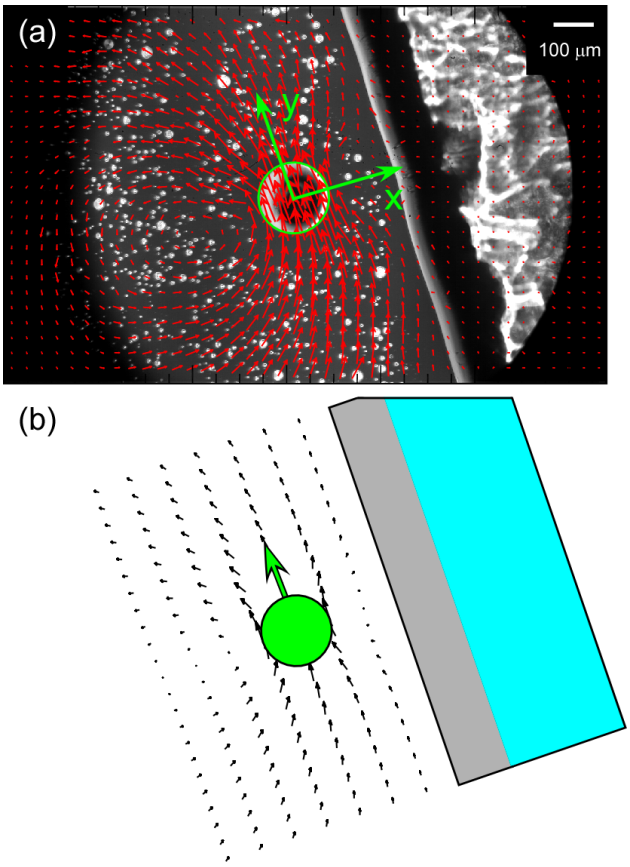

Figure 2.7: Experimental (a) and theoretical (b) flow fields for a post of radius 3.58 l_S moving parallel to a straight boundary at a distance of 232 μm (10.32 l_S). The gray box in (b) represents the location of the film meniscus, and the cyan box represents the actual glass film holder. We treat the edge of the meniscus as the beginning of the boundary; it is essentially rigid, since fluid in the uniform center of the film can not flow into it.

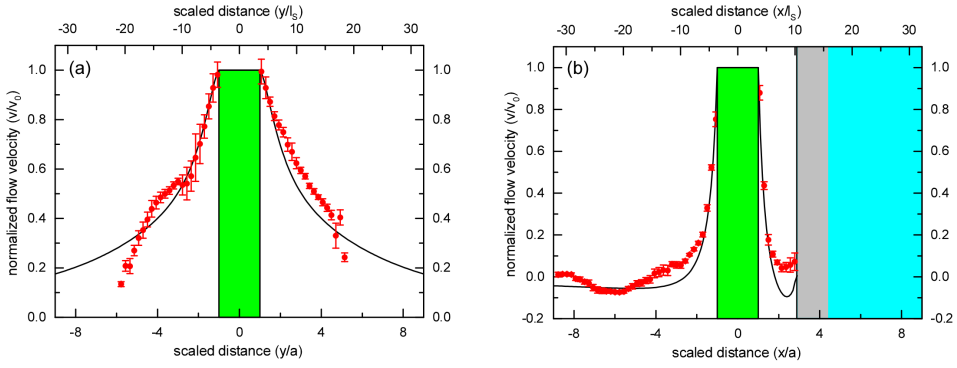

Figure 2.8: Velocity scans along y (a) and x (b) for a post in the same situation as Fig. 2.7. Note the imposed boundary condition that the predicted LM velocity go to zero at the edge of the meniscus.

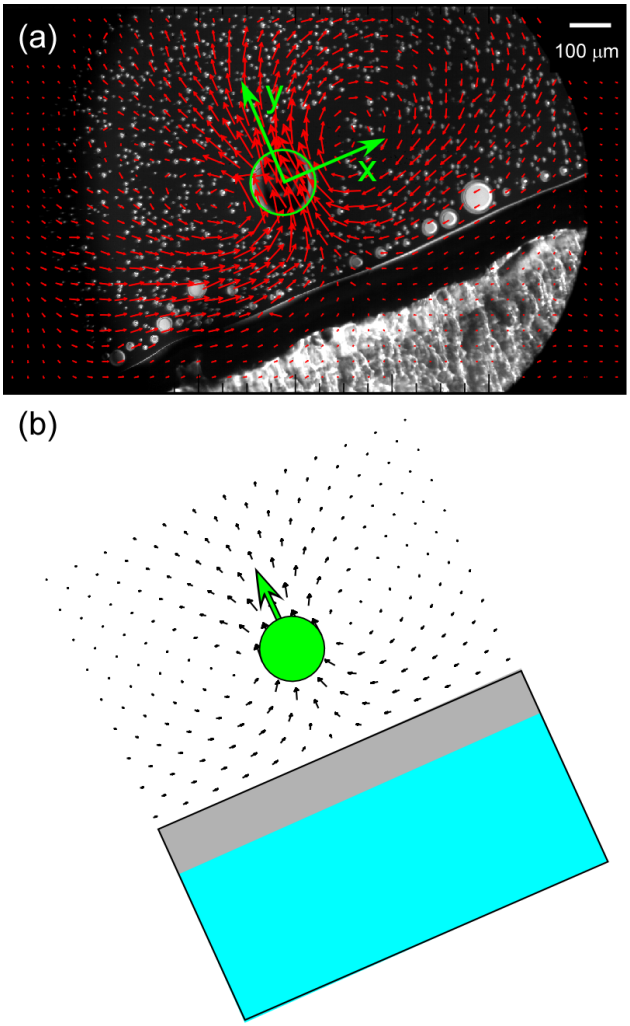

Figure 2.9: Experimental (a) and theoretical (b) flow fields for a post of radius 5.59 l_S moving perpendicular to a straight boundary at a distance of 258 μm (19.10 l_S). The gray box in (b) represents the location of the film meniscus, and the cyan box represents the actual glass film holder. We treat the edge of the meniscus as the beginning of the boundary; it is essentially rigid, since fluid in the uniform center of the film can not flow into it.

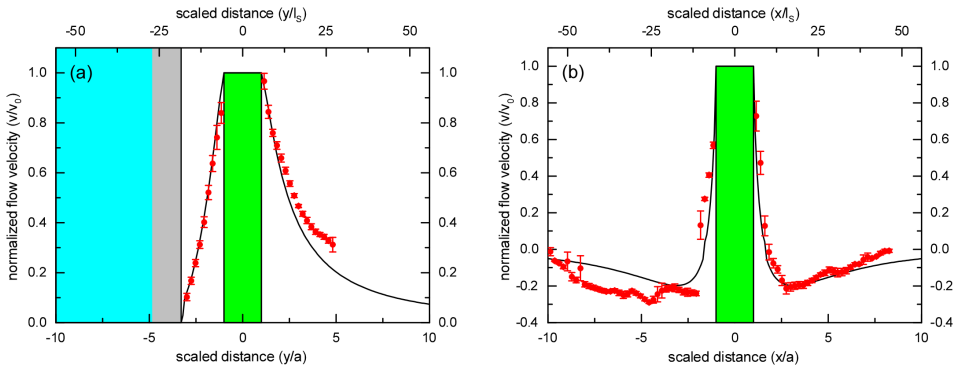

Figure 2.10: Velocity scans along y (a) and x (b) for a post in the same situation as Fig. 2.9. Note the imposed boundary condition that the predicted LM velocity go to zero at the edge of the meniscus.

Note that in both cases, the velocity does become negative; that is, we both predict and observe recirculation to occur. This is especially apparent for the post moving perpendicular to the edge, as fluid must move back to make room for the fluid that is pushed into the boundary. In general, the agreement between theory and experiment is much better for these two cases than for the cases of the post moving far from a boundary. This is because the flow in the air is subject to the same no-slip boundary conditions as the flow in the film. Thus, the air flow falls off much quicker than it does in the center of the film, and there is not as much room for momentum exchange between the two fluids.

2.4 Conclusion

We have performed an experiment in which a post is oscillated laterally in an 8CB film and the resulting flow field is mapped. Observations were compared to predictions made by a generalized LM theory. Results are consistent with the idea that the post extending beneath the film excites additional flow in the air, boosting the observed flow in the film.

Chapter 3

Mapping the Flow Field Generated by a Thin Nozzle Injecting Fluid into a Large Reservoir

In this chapter, I discuss another experiment in which I mapped the flow field generated by a thin nozzle injecting a smectic LC into a large reservoir of the material and compared the results to a theoretical model. Though the theoretical treatment of this geometry is well understood, and even often used as an example of implementing 2D Navier-Stokes Equations in textbooks [31, 26], this is the first experimental visualization performed for flow fields of this geometry. In addition, results allow us to better determine when a thin fluid is truly in the 2D regime, and when it is more quasi-2D.

3.1 Theoretical Model

The solution to the flow field generated by an infinitesimally thin nozzle injecting fluid at a constant rate into an infinite reservoir is a straightforward application of the 2D Navier-Stokes Equations: the continuity equation,

$$\frac{\partial v_x}{\partial x} + \frac{\partial v_y}{\partial y} = 0, \tag{3.1}$$

and the momentum equation,

$$v_x \frac{\partial v_x}{\partial x} + v_y \frac{\partial v_x}{\partial y} = \nu \frac{\partial^2 v_x}{\partial y^2}, \tag{3.2}$$

where v_i are the velocity components and ν is the kinematic viscosity. Note that the nozzle is taken to sit at the origin and point in the positive x-direction. Only two assumptions are made. The first is that the velocity of the fluid approaches zero as y (the distance perpendicular to the direction of the nozzle) approaches infinity. The second is that the nozzle acts as a constant momentum source,

$$M = \rho \int_{-\infty}^{+\infty} v_x^2 \, dy, \tag{3.3}$$

such that the momentum flux along the entire y-line is constant and independent of x.

Once these two assumptions are implemented, the Navier-Stokes Equations can be solved approximately in the high Re regime [16], with the flow velocity components given by:

$$v_x = \left(\frac{3M^2}{32\rho^2 \nu x} \right)^{1/3} \mathrm{sech}^2 \xi \tag{3.4}$$

and

$$v_y = \left(\frac{M\nu}{6\rho x^2} \right)^{1/3} (2\xi \mathrm{sech}^2 \xi - \tanh^2 \xi), \tag{3.5}$$

where

$$\xi = \left(\frac{M}{48\rho\nu^2} \right)^{1/3} \frac{y}{x^{2/3}}. \tag{3.6}$$

This flow field is plotted (with arbitrary units) in Fig. 3.1. The nozzle sits at the point $(0, 0)$.

3.2 Experiment

In order to test this geometry, a more complex film holder was needed than either the circular or rectangular ones used in the previous experiment. We created a film holder with racetrack geometry, shown in Fig. 3.2. Air is blown at a controlled speed through a needle beneath the film near the location of the red arrow. This generates the long-range flow necessary. As the fluid travels around the track, it is funneled through the thin nozzle in the upper right, then injected

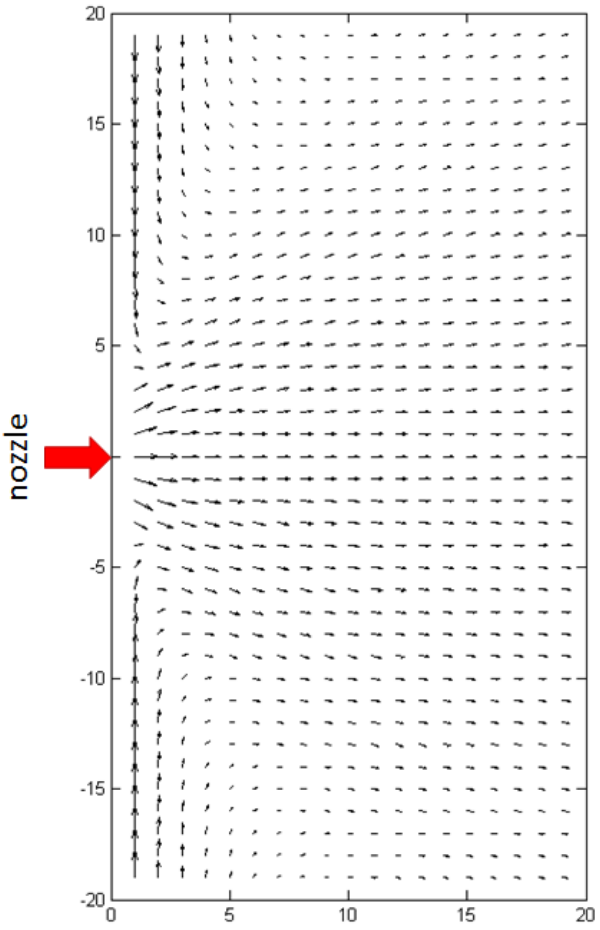

Figure 3.1: The predicted flow field for an infinitesimally thin nozzle acting as a constant momentum source for an infinitely large reservoir of 2D fluid. The nozzle sits at the point $(0, 0)$.

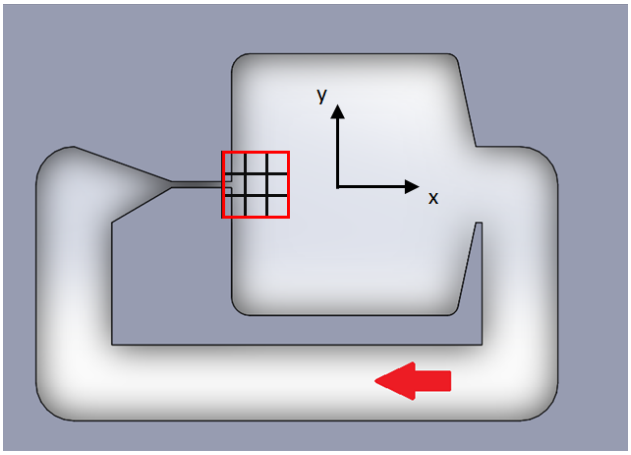

Figure 3.2: The film holder used in the nozzle experiment. A thin needle is used to blow on the film, exciting flow in the direction of the red arrow. The nozzle is 0.5 mm wide, and the reservoir is 21 mm wide by 20 mm long. The red box represents the area observed underneath the microscope. Because this area is larger than the camera's field of view, we take 9 separate videos and stitch the flow fields together in MATLAB.

into the large reservoir. The size and shape of the reservoir were designed such that any vorticity in the flow does not affect the flow field in the area observed, allowing us to treat the reservoir as essentially infinite. The entire setup is housed inside a vacuum chamber, so the experiment can be performed at different pressures. Note that while a true vacuum cannot be achieved due to the use of blown-in air to excite flow in the first place, the pressure can still be regulated as we reach an equilibrium between the air blown in through the needle and the air pumped out by the vacuum motor.

Rather than use 8CB for this experiment, we used a material called MX 12805, a multi-component Displaytech LC mixture which has the following phase diagram: Isotropic $\rightarrow$ (84.7 – 82 °C) $\rightarrow$ Nematic $\rightarrow$ (81.4 °C) $\rightarrow$ Smectic A $\rightarrow$ (66.1 °C) $\rightarrow$ Smectic C. Thus, it is in the SmC phase at room temperature. MX 12805 films are generally more stable than 8CB films, which makes them useful for drawing the larger films required for this experiment. Additionally, MX 12805 spontaneously generates islands, making it useful for working in vacuum chambers. It is difficult to generate islands by ash particle deposition in this case, because one must deposit the ash particles before moving the film into the vacuum chamber. The presence of ash particles in the

film makes it less stable, and thus more likely to pop when the surrounding air is disturbed.

Part of what makes this experiment challenging is that we are mapping flow over such a large area, rather than over an area local to the source of the flow. In order to capture the entire region of interest, nine videos were captured in a 3×3 square (shown in Fig. 3.2), each sub-region separated by a distance of 2 mm. Each video comprised approximately 200 frames at 60 frames-per-second. An XY-stage was used to shift between different sub-regions; it was controlled using the open-source program Micro-Manager [7]. An open-source particle imaging velocimetry program, OpenPIV [33], was used to map the flow field in each sub-region by tracking the motion of islands in the film. A MATLAB script that I wrote then averaged the flow field over all frames in each sub-region and stitched the 9 averaged fields together into one large field. Because the field-of-view in a single sub-region was larger than the separation between sub-regions, there was some overlap between each video (approximately forty percent of the field of view in the y-direction and ten percent in the x-direction). The area of overlap was split in half, with half of the data used coming from one sub-region and half from the other.

3.3 Results

Again, it is difficult to compare the entire observed flow field to that predicted by theory. Rather, I examined only the flow along the characteristic line exiting straight from the center of the nozzle. Along this line, there is only an x-component of the velocity, and it simplifies from the complicated expression above to

$$v_x = \left(\frac{3M^2}{32\rho^2 \nu x} \right)^{1/3}. \tag{3.7}$$

MX 12805 has density $\rho = 980$ kg/m^3 and kinematic viscosity $\nu = 6.33 \times 10^{-5}$ m^2/s. M, however, is not a property of the material but is dependent upon the speed at which fluid is being injected from the nozzle. It is set as a free parameter and determined by fitting the model to the experimental data. Velocity vs. distance from the nozzle along this center line is plotted for a film at atmospheric

pressure ($\sim$ 625 torr) in Fig. 3.3. The solid black curve represents the theoretical model prediction (using the best-fit M), and the red points represent experimental data.

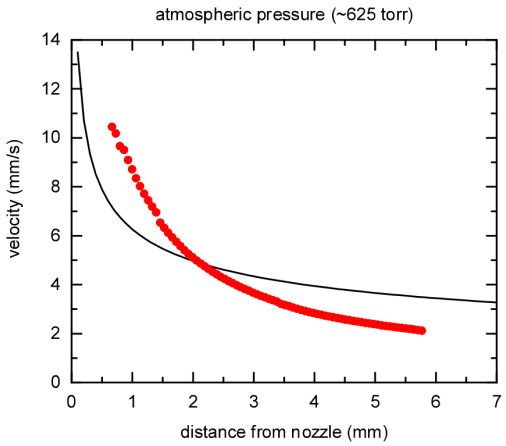

Figure 3.3: Velocity is plotted as a function of parallel distance from the nozzle for the case of a film at atmospheric pressure ($\sim$ 625 torr). The red points represent experimental data, and the solid black curve represents the theoretical model. We note that the predicted behavior falls off slower than the observed behavior. It is assumed that this is due to coupling between the film and the air that is not accounted for in the theory.

It is apparent that the predicted velocities fall off slower with distance than the observed ones do. It is assumed that this is due to coupling with the air that the model does not account for. Although this proved difficult to test in the moving post experiment of Chapter 2, the geometry of the equipment for this experiment makes it much easier to house everything in a vacuum chamber. We perform the experiment again at a variety of pressures. Because it is difficult to keep the air blowing in and the air pumped out at an exact equilibrium, each set of data was taken over a small range of pressures; however, these ranges are small enough to not noticeably affect the physics. Velocity vs. distance from the nozzle is plotted for 2 different pressures in Fig. 3.4.

We do experience two main experimental problems at reduced pressure. The first is that the film tends to deform and become non-planar near the nozzle. This out-of-plane bending creates dark regions in the film, where the reflected light from the microscope is not directed back up towards the objective lens. While this happens at all pressures, it becomes more pronounced at lower pressures, and extends over a larger area, as can be seen in Fig. 3.5. However, this serves

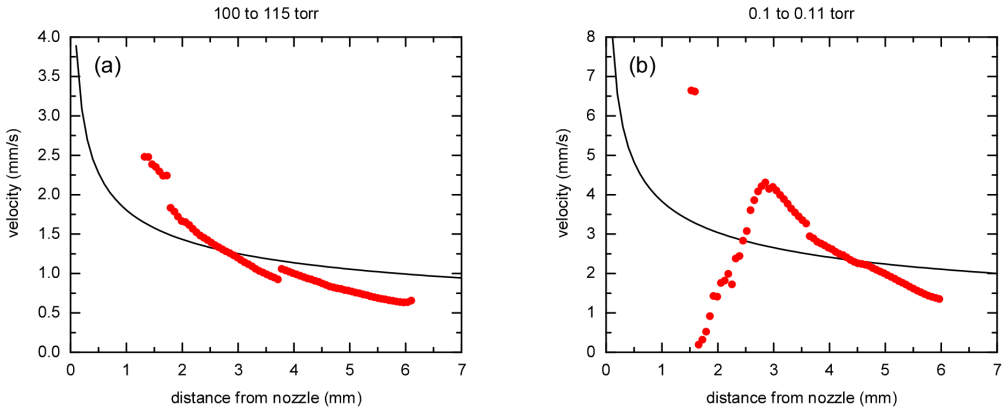

Figure 3.4: Velocity is plotted as a function of parallel distance from the nozzle for films at different pressures. Data at lower pressures appears noisier because there are small perturbations caused by the pumping out of air by the vacuum. Additionally, out-of-plane bending near the nozzle increases in area for lower pressures, so the observed flow fields begin farther from the nozzle.

only to lessen the region over which we can observe flow; it does not affect the flow itself by any measurable amount. The second problem is that the data tends to become noisier as the pressure goes down, with an apparent oscillatory behavior emerging. It is difficult to determine if this is a real effect, or simply a failure of the OpenPIV program to accurately determine the velocity just beyond the dark regions, where the image is still somewhat blurry.

Perhaps counter-intuitively, it does not appear that the theoretical model explains the behavior any better as the pressure decreases. We note a few different reasons for this. First, as SD showed, it is not the pressure of the bulk 3D fluid that matters, but the viscosity. The viscosity of air does not noticeably change between the range of $0.1 - 625$ torr [11], so we do not expect to see much change in behavior. Additionally, the theoretical solution assumes a high Reynolds number; unfortunately, the highest Reynolds number we achieved was $\mathrm{Re} \approx 1$, so we do not expect the model to be accurate in this regime. Lastly, the nozzle is not a point source (as assumed in our model), and flow across the nozzle itself is non-uniform, further contributing to the discrepancy.

Future work will focus on improving the experimental setup so that lower pressures can be achieved and true 2D behavior can be observed. Additionally, we are currently developing a process to achieve high-Re flow, and we hope to be able to truly probe the high-Re regime soon. A new film-

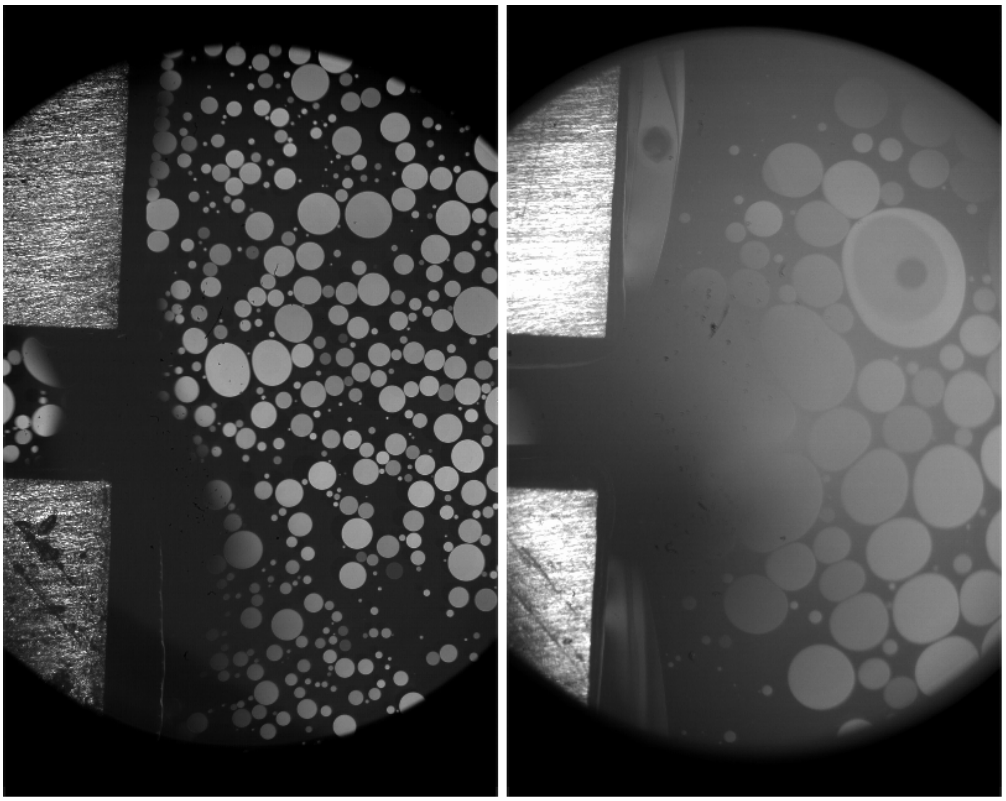

Figure 3.5: Out-of-plane bending near mouth of nozzle. The image on the left shows the film at atmospheric pressure, and the image on the right shows the film at 0.1 torr. Note that despite a longer exposure time, the image on the right still has a larger region that appears darker. While this bending does not appear to affect the flow, it does make it more difficult for OpenPIV to accurately determine the velocity just outside the dark regions.

holder has been machined with a smaller nozzle, which should make the assumption of a point-sized nozzle more accurate. In the case that these developments do not yield better agreement between model and experiment, we plan to update our theoretical treatment of the system to better account for the discrepancies between the two.

3.4 Conclusion

We have mapped the flow field generated by a thin 2D nozzle injecting fluid into a large reservoir at multiple pressures, and compared the observations to predictions made by the 2D Navier-Stokes Equations. The work was performed at multiple pressures in order to probe when the films start behaving as true 2D fluids rather than quasi-2D fluids. Results imply that this crossover does not occur above pressures of 0.1 torr, though a more refined experiment and model would help to strengthen this conclusion.

Bibliography

[1] Andrew R. Barron. Physical Methods in Chemistry and Nano Science. Rice University, 2012.

[2] Howard Brenner. The slow motion of a sphere through a viscous fluid towards a plane surface. Chemical Engineering Science, 16(3):242–251, December 1961.

[3] Mauricio D. Carbajal-Tinoco, Ricardo Lopez-Fernandez, and Jos Luis Arauz-Lara. Asymmetry in Colloidal Diffusion near a Rigid Wall. Physical Review Letters, 99(13):138303, September 2007.

[4] Peter J. Collings and Michael Hird. Introduction to Liquid Crystals: Chemistry and Physics. CRC Press, March 1997.

[5] Bianxiao Cui, Haim Diamant, Binhua Lin, and Stuart A. Rice. Anomalous Hydrodynamic Interaction in a Quasi-Two-Dimensional Suspension. Physical Review Letters, 92(25):258301, June 2004.

[6] D. Davidov, C. R. Safinya, M. Kaplan, S. S. Dana, R. Schaetzing, R. J. Birgeneau, and J. D. Litster. High-resolution x-ray and light-scattering study of critical behavior associated with the nematicsmectic-A transition in 4-cyano-4-octylbiphenyl. Physical Review B, 19(3):1657–1663, February 1979.

[7] Arthur D Edelstein, Mark A Tsuchida, Nenad Amodaj, Henry Pinkard, Ronald D Vale, and Nico Stuurman. Advanced methods of microscope control using Manager software. Journal of Biological Methods, 1(2):10, November 2014.

[8] edited by R. C. Weast. Handbook of Chemistry and Physics. CRC Press, Cleveland, 54th edition, 1973.

[9] A. Eremin, S. Baumgarten, K. Harth, R. Stannarius, Z. H. Nguyen, A. Goldfain, C. S. Park, J. E. Maclennan, M. A. Glaser, and N. A. Clark. Two-Dimensional Microrheology of Freely Suspended Liquid Crystal Films. Physical Review Letters, 107(26):268301, December 2011.

[10] O. H. Faxen. Forces Exerted on a Rigid Cylinder in a Viscous Fluid Between Two Parallel Fixed Plates. Royal Swedish Academy of Engineering Science, 1946.

[11] Daniel Grieser and William Goldthwaite. EXPERIMENTAL DETERMINATION OF THE VISCOSITY OF AIR IN THE GASEOUS STATE AT LOW TEMPERATURES AND PRESSURES. Technical Report AEDC-TDR-63-143, U.S. Air Force.

[12] J. Happel and H. Brenner. Low Reynolds number hydrodynamics: with special applications to particulate media. Springer Science & Business Media, December 2012.

[13] B. D. Hughes, B. A. Pailthorpe, and L. R. White. The translational and rotational drag on a cylinder moving in a membrane. Journal of Fluid Mechanics, 110:349–372, September 1981.

[14] A. J. Leadbetter, J. L. A. Durrant, and M. Rugman. The Density Of 4 n-Octyl-4-Cyano-Biphenyl (8cb). Molecular Crystals and Liquid Crystals, 34(10):231–235, October 1976.

[15] Alex J. Levine and F. C. MacKintosh. Dynamics of viscoelastic membranes. Physical Review E, 66(6):061606, December 2002.

[16] C. C. Mei. Two dimensional laminar jet. MIT Course Lecture Notes.

[17] Zoom Hoang Nguyen, Markus Atkinson, Cheol Soo Park, Joseph Maclennan, Matthew Glaser, and Noel Clark. Crossover between 2d and 3d Fluid Dynamics in the Diffusion of Islands in Ultrathin Freely Suspended Smectic Films. Physical Review Letters, 105(26):268304, December 2010.

[18] Naomi Oppenheimer and Haim Diamant. Correlated Diffusion of Membrane Proteins and Their Effect on Membrane Viscosity. Biophysical Journal, 96(8):3041–3049, April 2009.

[19] Naomi Oppenheimer and Haim Diamant. In-Plane Dynamics of Membranes with Immobile Inclusions. Physical Review Letters, 107(25):258102, December 2011.

[20] Patrick Oswald and Pawel Pieranski. Nematic and Cholesteric Liquid Crystals: Concepts and Physical Properties Illustrated by Experiments. CRC Press, February 2005.

[21] Patrick Oswald and Pawel Pieranski. Smectic and Columnar Liquid Crystals: Concepts and Physical Properties Illustrated by Experiments. CRC Press, December 2005.

[22] Mattia Felice Palermo, Luca Muccioli, and Claudio Zannoni. Molecular organization in freely suspended nano-thick 8cb smectic films. An atomistic simulation. Physical Chemistry Chemical Physics, 17(39):26149–26159, September 2015.

[23] G. S. Perkins and R. B. Jones. Hydrodynamic interaction of a spherical particle with a planar boundary II. Hard wall. Physica A Statistical Mechanics and its Applications, 189:447–477, November 1992.

[24] Eugene P. Petrov, Rafayel Petrosyan, and Petra Schwille. Translational and rotational diffusion of micrometer-sized solid domains in lipid membranes. Soft Matter, 8(29):7552–7555, July 2012.

[25] Eugene P. Petrov and Petra Schwille. Translational Diffusion in Lipid Membranes beyond the Saffman-Delbrck Approximation. Biophysical Journal, 94(5):L41–L43, March 2008.

[26] David Pnueli and Chaim Gutfinger. Fluid Mechanics. Cambridge University Press, January 1997.

[27] V. Prasad and Eric R. Weeks. Flow fields in soap films: Relating viscosity and film thickness. Physical Review E, 80(2):026309, August 2009.

[28] Zhiyuan Qi, Zoom Hoang Nguyen, Cheol Soo Park, Matthew A. Glaser, Joseph E. Maclennan, Noel A. Clark, Tatiana Kuriabova, and Thomas R. Powers. Mutual Diffusion of Inclusions in Freely Suspended Smectic Liquid Crystal Films. Physical Review Letters, 113(12):128304, September 2014.

[29] Friedrich Reinitzer. Beitrge zur Kenntniss des Cholesterins. Monatshefte fr Chemie und verwandte Teile anderer Wissenschaften, 9(1):421–441, December 1888.

[30] P. G. Saffman and M. Delbrck. Brownian motion in biological membranes. Proceedings of the National Academy of Sciences, 72(8):3111–3113, August 1975.

[31] Herrmann Schlichting and Klaus Gersten. Boundary-Layer Theory. Springer Science & Business Media, May 2003.

[32] F. Schneider. Measurement of the viscosity coefficient 3 in free-standing smectic films. Physical Review E, 74(2):021709, August 2006.

[33] Z. J. Taylor, R. Gurka, G. A. Kopp, and A. Liberzon. Long-Duration Time-Resolved PIV to Study Unsteady Aerodynamics. IEEE Transactions on Instrumentation and Measurement, 59(12):3262–3269, December 2010.